



# Vector modulation instability in birefringent graded-index multimode fibers

AMIRA S. AHSAN<sup>1,\*</sup>  AND GOVIND P. AGRAWAL<sup>1,2</sup> 

<sup>1</sup>The Institute of Optics, University of Rochester, Rochester, New York 14627, USA

<sup>2</sup>Laboratory for Laser Energetics, University of Rochester, Rochester, New York 14623, USA

\*Corresponding author: aahsan@ur.rochester.edu

Received 12 October 2020; revised 16 November 2020; accepted 17 November 2020; posted 17 November 2020 (Doc. ID 412450); published 14 December 2020

We study vectorial modulation instability occurring inside a birefringent graded-index (GRIN) fiber when the two polarization components of the optical field are coupled nonlinearly through cross-phase modulation. In the scalar case in which only modes of one polarization are excited, the geometric parametric instability is known to produce an infinite number of sidebands around the wavelength of the input optical beam. We show that the birefringence of a GRIN fiber splits each of these sidebands into a triplet, whose frequency spacing depends on the differential group delay between the orthogonally polarized components. We verify the predictions of the linear stability analysis numerically by solving two coupled nonlinear Schrödinger equations that include spatial self-imaging effects through an effective nonlinear parameter. We present results for both continuous and pulsed optical beams experiencing normal or anomalous group-velocity dispersion inside a GRIN fiber. © 2020 Optical Society of America

<https://doi.org/10.1364/JOSAB.412450>

## 1. INTRODUCTION

The nonlinear phenomenon of modulation instability (MI) has been extensively studied in the context of nonlinear fiber optics [1]. In the case of single-mode fibers, MI occurs when the input beam experiences anomalous group-velocity dispersion (GVD), and it leads to temporal modulation of an intense continuous wave (CW) as it propagates down the fiber. In the spectral domain, this leads to the generation of two sidebands on the opposite sides of the CW's central frequency. This picture changes drastically in the case of a graded-index (GRIN) fiber because of the self-imaging property of such fibers that leads to periodic spatial variations in an optical beam's size as it propagates down the fiber [2].

As early as 2003, it was found that the MI creates an infinite number of sideband pairs, irrespective of whether the GVD is normal or anomalous at the wavelength of the incident CW Gaussian beam [3]. This kind of MI is called geometric parametric instability, and it was studied extensively after 2015, both theoretically and experimentally [4–7]. Its physical origin is related to the phenomenon of self-imaging [2]. Periodic spatial variations create through the Kerr effect a periodically varying refractive index along the length of a GRIN fiber, producing a kind of nonlinear Bragg grating. This grating provides quasi-phase matching for spatiotemporal instability, resulting in the generation of multiple pairs of spectral sidebands at specific wavelengths on both sides of the input beam's wavelength. Other noteworthy studies include MI in a few-mode step-index

fiber [8,9], a few-mode GRIN fiber [10], and a GRIN fiber with an axially modulated core diameter [11].

It is well known in the case of single-mode fibers that MI is affected considerably by the fiber's birefringence [12–17]. This type of MI is called vectorial because it involves the vector nature of the electric field through coupling between its two polarization components. However, to the best of our knowledge, vectorial MI occurring inside a birefringent GRIN fiber has not been considered before. In this paper, we study the vectorial MI inside such a fiber when both polarization components of the fiber's modes are excited and are coupled nonlinearly through cross-phase modulation (XPM). We show that birefringence of the GRIN fiber splits each sideband into a triplet, whose frequency spacing depends on the differential group delay (DGD) between the orthogonally polarized components. We verify the predictions of our linear stability analysis numerically by solving two coupled nonlinear Schrödinger (NLS) equations that include spatial self-imaging effects through an effective nonlinear parameter.

## 2. COUPLED NLS EQUATIONS

The refractive index of a birefringent GRIN fiber in the parabolic-index approximation takes the form [18]

$$n_j^2(\rho) = n_{0j}^2[1 - 2\Delta(\rho/a)^2] + n_2I, \quad \rho = \sqrt{x^2 + y^2}, \quad (1)$$

where  $j = x, y$ , and  $n_{0x}$  and  $n_{0y}$  represent the refractive index along the  $x$  and  $y$  directions, respectively, at the center of the fiber's core of radius  $a$ . Their values are different because of the stress applied along the  $x$  direction. It is useful to define an average value as  $n_0 = (n_{0x} + n_{0y})/2$ . The relative index difference is then given by  $\Delta = (n_0 - n_c)/n_0$ , where  $n_c$  is the cladding's refractive index. The last term in Eq. (1) represents the nonlinear contribution, which depends on the local intensity  $I$  and the Kerr coefficient  $n_2$  (about  $3.2 \times 10^{-20}$  m<sup>2</sup>/W for silica glass).

Although a modal description is often used for GRIN fibers, it becomes too complicated when the fiber supports a large number of modes, especially when birefringence is induced through an elliptical core. We do not employ the modal picture in this paper. We consider a pulsed optical beam with its spectrum centered at the frequency  $\omega_0$ . It is launched into the GRIN fiber such that its polarization direction makes an angle from the  $x$  axis. The electric field at any point inside the birefringent GRIN fiber can then be written as

$$\mathbf{E}(\mathbf{r}, t) = \text{Re}(\hat{x} E_x e^{i(\beta_{0x} - i\omega_0 t)} + \hat{y} E_y e^{i(\beta_{0y} - i\omega_0 t)}), \quad (2)$$

where  $E_x$  and  $E_y$  are the amplitudes of the  $x$  and  $y$  polarized components, respectively. The propagation constants,  $\beta_{0x}$  and  $\beta_{0y}$ , are defined as  $\beta_{0j} = \omega_0 n_{0j}/c$ , where  $c$  is the speed of light in vacuum. Using Maxwell's equations, the spatiotemporal evolution of the pulsed beam is found to be governed by the following two coupled equations [1, 19]:

$$\begin{aligned} \frac{\partial E_x}{\partial z} = & \frac{i}{2\beta_0} \nabla_T^2 E_x - \beta_{1x} \frac{\partial E_x}{\partial t} - i \frac{\beta_2}{2} \frac{\partial^2 E_x}{\partial t^2} - i \beta_0 \Delta \frac{\rho^2}{a^2} E_x \\ & + i \frac{n_2 \omega_0}{c} \left[ \left( |E_x|^2 + \frac{2}{3} |E_y|^2 \right) E_x + \frac{1}{3} E_x^* E_y^2 e^{-i2\Delta\beta z} \right], \end{aligned} \quad (3)$$

$$\begin{aligned} \frac{\partial E_y}{\partial z} = & \frac{i}{2\beta_0} \nabla_T^2 E_y - \beta_{1y} \frac{\partial E_y}{\partial t} - i \frac{\beta_2}{2} \frac{\partial^2 E_y}{\partial t^2} - i \beta_0 \Delta \frac{\rho^2}{a^2} E_y \\ & + i \frac{n_2 \omega_0}{c} \left[ \left( |E_y|^2 + \frac{2}{3} |E_x|^2 \right) E_y + \frac{1}{3} E_y^* E_x^2 e^{i2\Delta\beta z} \right], \end{aligned} \quad (4)$$

where  $\nabla_T^2$  is the transverse Laplacian operator, and  $\beta_0 = (\beta_{0x} + \beta_{0y})/2$ . These equations assume that the difference  $\Delta\beta = \beta_{0x} - \beta_{0y}$  is so small that we can replace  $\beta_{0x}$  and  $\beta_{0y}$  with their average value  $\beta_0$ . This assumption is valid in practice even for the so-called highly birefringent fibers because the ratio  $\Delta\beta/\beta_0$  remains below  $10^{-4}$ . Different group velocities of the two polarization components are included through  $v_{gj} = 1/\beta_{1j}$ , with  $j = x, y$ . Their difference is related to the DGD parameter defined as  $d = \beta_{1x} - \beta_{1y}$ . The GVD parameter  $\beta_2$  is the same for both polarization components. The three nonlinear terms govern the effects of self-phase modulation (SPM), XPM, and intermodal four-wave mixing (FWM). Note that the FWM term still depends on the fiber's birefringence through  $\Delta\beta$ .

Equations (3) and (4) include all spatial and temporal effects and require long computation time because of their four-dimensional nature. They can be simplified considerably with a variational approach [19]. In the case of a CW Gaussian beam,

the time derivatives vanish, and these equations can be solved using a variational technique outlined in Ref. [20]. Assuming that spatial evolution is not affected by the pulse nature of the beam, we make the approximation

$$E_j(\mathbf{r}, t) \approx F(x, y, z) A_j(z, t), \quad (j = x, y), \quad (5)$$

where  $A_j(z, t)$  is the slowly varying pulse envelope and  $F(x, y, z)$  governs periodic spatial variations of the Gaussian beam along the fiber's length owing to self-imaging. This equation assumes that the spatial self-imaging pattern is the same for both polarization components. This is a common assumption and is expected to be valid for most fibers. For a pulsed Gaussian beam with peak powers below the self-focusing threshold, the beam maintains its self-imaging nature inside GRIN fibers [19]. The spatial evolution of a Gaussian beam is then governed by [20]

$$F(x, y, z) = \frac{w_0}{w(z)} \exp \left[ -\frac{\rho^2}{2w(z)} \right], \quad (6)$$

where the beam waist  $w(z)$  varies with  $z$  in a periodic manner as

$$w(z) = w_0 \sqrt{\cos^2(\pi z/z_p) + C^2 \sin^2(\pi z/z_p)}. \quad (7)$$

Here  $w_0$  is the  $1/e$  width of the input Gaussian beam (full width at half maximum is  $1.665w_0$ ), and the parameters  $z_p$  and  $C$  are defined as

$$z_p = \frac{\pi a}{\sqrt{2\Delta}}, \quad C = z_p/(\beta_0 \pi w_0^2). \quad (8)$$

Physically,  $z_p$  represents the self-imaging period, and  $C$  is the compression factor by which the beam width is reduced in the middle of each self-imaging cycle. For a typical GRIN fiber,  $z_p < 1$  mm, and  $C \sim 0.1$  can be varied by changing  $w_0$ .

We can simplify Eqs. (3) and (4) considerably by using Eq. (5), multiplying the result with  $F^*(x, y, z)$ , and integrating over the transverse coordinates [19]. This procedure eliminates the  $x$  and  $y$  dependence and results in two coupled NLS equations given by

$$\begin{aligned} \frac{\partial \Psi_x}{\partial z} + \beta_{1x} \frac{\partial \Psi_x}{\partial t} + i \frac{\beta_2}{2} \frac{\partial^2 \Psi_x}{\partial t^2} \\ = i \gamma(z) \left[ \left( |\Psi_x|^2 + \frac{2}{3} |\Psi_y|^2 \right) \Psi_x + \frac{1}{3} \Psi_x^* \Psi_y^2 e^{-i2\Delta\beta z} \right], \end{aligned} \quad (9)$$

$$\begin{aligned} \frac{\partial \Psi_y}{\partial z} + \beta_{1y} \frac{\partial \Psi_y}{\partial t} + i \frac{\beta_2}{2} \frac{\partial^2 \Psi_y}{\partial t^2} \\ = i \gamma(z) \left[ \left( |\Psi_y|^2 + \frac{2}{3} |\Psi_x|^2 \right) \Psi_y + \frac{1}{3} \Psi_y^* \Psi_x^2 e^{i2\Delta\beta z} \right], \end{aligned} \quad (10)$$

where  $\Psi_j = \sqrt{S} A_j$  is normalized with the area  $S(z) = \iint_{-\infty}^{\infty} |F(x, y, z)|^2 dx dy$  such that  $|\Psi_j|^2$  represents the optical power. The self-imaging effects appear in these equations through the  $z$  dependence of the nonlinear parameter  $\gamma$  defined as

$$\gamma(z) = \frac{n_2 \omega_0}{c A_{\text{eff}}(z)} = \frac{\gamma_0}{f(z)}, \quad f(z) = \frac{A_{\text{eff}}(z)}{A_{\text{eff}}(0)}, \quad (11)$$

where the  $z$ -dependent effective area is defined as

$$A_{\text{eff}}(z) = S^2(z) / \left( \iint_{-\infty}^{\infty} |F(x, y, z)|^4 dx dy \right). \quad (12)$$

The function  $f(z)$  represents the factor by which the effective area  $A_{\text{eff}}(z)$  changes at a distance  $z$  from its initial value at  $z = 0$ . This function is also periodic in  $z$  with the period  $z_p$ .

It is useful for numerical purposes to normalize this set of equations by introducing the following dimensionless variables [1]:

$$U_x = \Psi_x / \sqrt{P_0}, \quad U_y = \Psi_y / \sqrt{P_0}, \\ \xi = z / L_{\text{NL}}, \quad \tau = (t - \bar{\beta}_1 \xi) / T_0, \quad (13)$$

where  $P_0$  is the peak power of the input pulse launched into the fiber, and the nonlinear length is defined as  $L_{\text{NL}} = (\gamma_0 P_0)^{-1}$ . The average group delay is defined as  $\bar{\beta}_1 = (\beta_{1x} + \beta_{1y})/2$ , and  $\tau$  is the time in a frame moving at this group velocity and normalized using  $T_0 = \sqrt{|\beta_2| L_{\text{NL}}}$ . Equations (9) and (10) now take the form

$$\frac{\partial U_x}{\partial \xi} + \frac{\sigma}{2} \frac{\partial U_x}{\partial \tau} + i \frac{s}{2} \frac{\partial^2 U_x}{\partial \tau^2} = i f^{-1}(\xi) \left[ (|U_x|^2 + \frac{2}{3} |U_y|^2) U_x \right], \quad (14)$$

$$\frac{\partial U_y}{\partial \xi} - \frac{\sigma}{2} \frac{\partial U_y}{\partial \tau} + i \frac{s}{2} \frac{\partial^2 U_y}{\partial \tau^2} = i f^{-1}(\xi) \left[ (|U_y|^2 + \frac{2}{3} |U_x|^2) U_y \right], \quad (15)$$

where  $s = \text{sgn}(\beta_2)$ , and  $\sigma = (\beta_{1x} - \beta_{1y}) L_{\text{NL}} / T_0$  is a measure of the DGD. We have ignored the FWM terms assuming that they are not phase matched because of the relatively large birefringence of the fiber [1]. The self-imaging effects are included in these equations through the periodic function  $f(\xi) = \cos^2(\pi q \xi) + C^2 \sin^2(\pi q \xi)$ , where  $q = L_{\text{NL}} / z_p$  is the ratio of the nonlinear length to the self-imaging period. This ratio exceeds 100 for even  $P_0 = 1$  kW because  $L_{\text{NL}} > 10$  cm while  $z_p < 1$  mm.

### 3. LINEAR STABILITY ANALYSIS

To discuss vectorial MI, we follow a standard procedure based on the linear stability analysis [1]. Equations (14) and (15) can be solved in the CW case (no time derivatives), and the solution is given as

$$U_x = \sqrt{P_x} \exp \left[ i \left( P_x + \frac{2}{3} P_y \right) \int_0^\xi f^{-1}(\xi') d\xi' \right], \quad (16)$$

$$U_y = \sqrt{P_y} \exp \left[ i \left( P_y + \frac{2}{3} P_x \right) \int_0^\xi f^{-1}(\xi') d\xi' \right], \quad (17)$$

where  $P_x = |U_x|^2 = \cos^2 \theta$  and  $P_y = |U_y|^2 = \sin^2 \theta$  are the relative powers of two polarization components such that  $P_x + P_y = 1$ . Here  $\theta$  is the polarization angle of the input beam from the slow axis of the fiber. Except for the nonlinear

phase shifts induced by SPM and XPM, the CW wave should remain unchanged as it propagates inside the GRIN fiber, if this solution is stable to perturbations.

In a linear stability analysis, we perturb the CW solution by replacing  $\sqrt{P_j}$  with  $\sqrt{P_j} + p_j(\xi, \tau)$ , where  $p_j$  is a small perturbation of the form

$$p_j(\xi, \tau) = a_j(\xi) e^{-i\Omega\tau} + b_j(\xi) e^{i\Omega\tau}, \quad (18)$$

and  $\Omega$  is the frequency of this perturbation. After linearizing the resulting equations in  $a_j$  and  $b_j$ , we obtain the following two linear ordinary differential equations:

$$\frac{\partial a_x}{\partial \xi} = \frac{i}{2} (\sigma \Omega + s \Omega^2) a_x + i f^{-1}(\xi) \\ \times \left[ P_x (a_x + b_x^*) + \frac{2}{3} \sqrt{P_x P_y} (a_y + b_y^*) \right], \quad (19)$$

$$\frac{\partial a_y}{\partial \xi} = \frac{i}{2} (-\sigma \Omega + s \Omega^2) a_y + i f^{-1}(\xi) \\ \times \left[ P_y (a_y + b_y^*) + \frac{2}{3} \sqrt{P_x P_y} (a_x + b_x^*) \right]. \quad (20)$$

A similar set of equations can be derived for  $\partial b_j / \partial \xi$ . These equations are linear but inhomogeneous because of the presence of  $f^{-1}(\xi)$ . However, they can still be solved by exploiting the periodic nature of the self-imaging phenomenon following the procedure in Ref. [21]. We first expand  $f^{-1}(\xi)$  in a Fourier series as

$$f^{-1}(\xi) = \sum_{m=-\infty}^{\infty} c_m \exp(i k_m \xi), \quad k_m = 2\pi q m, \quad (21)$$

where  $c_m$  are the Fourier coefficients. Close to a resonance with the  $p$ th Fourier component, we introduce the transformation  $a_j(\xi) = u_j(\xi) \exp[i(K + k_p/2)\xi]$  and  $b_j(\xi) = v_j(\xi) \exp[i(-K + k_p/2)\xi]$ , where  $K$  is the wave number of the perturbation. This results in an eigenvalue equation of the form  $[M][V] = K[V]$  for the eigenvector defined as  $[V]^T = [u_x, v_x^*, u_y, v_y^*]$ . The stability matrix  $[M]$  has the form

$$[M] = \begin{bmatrix} (A + B_x) & C_x & D_0 & D_p \\ -C_x^* & (A - B_x) & -D_p^* & -D_0 \\ D_0 & D_p & -(A - B_y) & C_y \\ -D_p^* & -D_0 & -C_y^* & -(A + B_y) \end{bmatrix}, \quad (22)$$

where  $A = \sigma \Omega / 2$ ,  $B_j = (s \Omega^2 - k_p) / 2 + c_0 P_j$ ,  $C_j = c_p P_j$ , and

$$D_0 = 2c_0 \sqrt{P_x P_y} / 3, \quad D_p = 2c_p \sqrt{P_x P_y} / 3. \quad (23)$$

The four eigenvalues of the stability matrix  $[M]$  are used to find the frequencies for which perturbation becomes unstable. If an eigenvalue  $K$  of the perturbation has a negative imaginary part, the corresponding eigenvector begins to grow exponentially with  $\xi$ , leading to instability of the CW solution. Using the form  $e^{iK\xi}$ , the power gain of MI is given by  $g(\Omega) = -2\text{Im}(K_m)$ , where  $K_m$  is the eigenvalue of the stability matrix in Eq. (22) with the highest negative imaginary part.

#### 4. VECTOR MI: NORMAL GVD

To discuss and compare our analytic and numerical results, we consider a standard GRIN fiber with the core radius  $a = 25 \mu\text{m}$  and  $\Delta = 0.009$ . As we present our results in normalized units, they can apply for a variety of input conditions. As an example, we consider a quasi-CW Gaussian beam at 1064 nm wavelength that is launched into the GRIN fiber with a spot size  $w_0 = 18 \mu\text{m}$  and 100 kW peak power. It is polarized linearly at an angle of  $45^\circ$  so that  $P_x = P_y = 50 \text{ kW}$ , and it propagates in the normal-GVD region ( $\beta_2 = 17 \text{ ps}^2/\text{km}$ ). The nonlinear length is 10.8 cm and the scaling time is  $T_0 = 43 \text{ fs}$  in this situation, but these can vary over a wide range for different input conditions. The parameters governing spatial-width oscillations are  $z_p = 592 \mu\text{m}$ ,  $C = 0.07$ , and  $q = 182$ . Our choice of  $\sigma = 5$  corresponds to a DGD of approximately 2 ps/m.

Using the preceding parameters, we first obtain the MI gain spectrum by using the stability matrix in Eq. (22) for different values of  $c_p$ . We verify the predictions of our theory by solving Eqs. (14) and (15) numerically in the frequency domain with the fourth-order Runge–Kutta method [22]. For each polarization component, the input field is  $U_j(0, \tau) = 0.5 + n_j(\tau)$  with  $j = x, y$ , where the noise  $n_j(\tau)$  is included in the frequency domain by adding a random quantity to each spectral component of  $U_j(0, \tau)$  with a random phase and a constant amplitude set at  $10^{-5}$  (noise power 100 dB below the input power level).

In Fig. 1, we show on top the gain spectrum obtained through our linear stability analysis. The bottom two traces show the spectra obtained numerically at a distance of  $1.5 L_{\text{NL}}$  (16 cm) for the  $x$ - and  $y$ -polarized components. When the input beam is orientated along the slow or fast axes of the GRIN fiber axes, only the frequencies shown by vertical dotted lines appear in the spectrum. This situation corresponds to the scalar case studied in the context of the geometric parametric instability [4–6]. The nonlinear grating induced by self-imaging creates an infinite number of sidebands, whose frequency shifts from the center frequency  $\omega_0$  are given by [5]

$$\Omega_p = \pm \sqrt{2s(\pi qp - c_0 P_j)}, \quad (j = x, y), \quad p = 0, \pm 1, \pm 2, \dots \quad (24)$$

We shall refer to these sidebands as nonlinear grating-induced (NGI) sidebands. In the case of normal GVD ( $s = 1$ ), the  $p = 0$  NGI sideband does not exist. However, when GVD is anomalous ( $s = -1$ ),  $p = 0$ , a sideband pair forms in addition to other pairs for  $p < 0$ .

It is now relatively easy to interpret the MI spectra in Fig. 1 for a birefringent GRIN fiber. The nonlinear grating induced by self-imaging still creates an infinite number of sidebands. The fiber's birefringence splits each of these sidebands into a triplet, because of the XPM-induced coupling between the orthogonally polarized beam components traveling at different speeds. The frequency separation of this triplet is relatively small, compared to the spacing of grating-induced sidebands, and depends on the DGD parameter  $\sigma$  and the polarization angle  $\theta$  of the input beam. The spacing becomes maximum for  $\theta = 45^\circ$  for which the two polarization components are equally intense. We shall refer to these as the XPM sidebands.

It is important to investigate the state of polarization (SOP) of the two XPM sidebands, located on opposite sides of each NGI sideband. For this purpose, we analyze the eigenvectors of

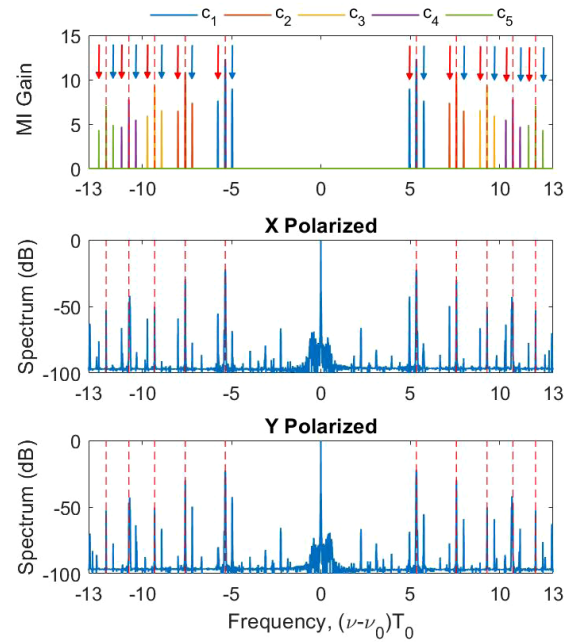


**Fig. 1.** MI Gain spectrum (top) from the linear stability matrix for a Gaussian beam propagating in the normal-GVD region of a birefringent GRIN fiber. Numerical results are shown below for the  $x$ - (middle) and  $y$ - (bottom) polarized components. Vertical dotted lines indicate the sideband frequencies predicted in the scalar case. Sidebands marked by the red and blue arrows are polarized along the  $x$  and  $y$  directions. See text for values of the parameters used.

the matrix  $M$  in Eq. (22). The eigenvector associated with each eigenvalue with a negative imaginary part describes the SOP of that specific frequency component. As one may expect, the NGI sidebands have the same SOP as that of the input beam. However, that is not the case for the XPM sidebands. Indeed, the eigenvector analysis shows that the red shifted sideband is  $x$  polarized, whereas the blue shifted sideband is  $y$  polarized. This is similar to how vector MI manifests in highly birefringent step-index fibers and is related to a phase-matched FWM process in which frequency shift of the XPM sidebands is balanced by the group-velocity mismatch [13].

The optical spectra, obtained by solving the coupled NLS equations numerically, are displayed in Fig. 1 for the  $x$ - (middle) and  $y$ - (bottom) polarized components. Several things are noteworthy when we compare these with the predictions of the linear stability analysis. First, the locations of the NGI sidebands are in agreement with the predictions based on Eq. (24) shown by the dotted vertical lines in Fig. 1. As expected, these sideband pairs are present on both polarization axes. Second, the XPM sidebands (forming a triplet) should be polarized along either the  $x$  or  $y$  axis. Numerical results indeed show that the spectral amplitudes of the two SPM sidebands are asymmetric and typically differ by more than 20 dB. The reason that the amplitude of the forbidden sideband does not vanish in numerical simulations is related to the presence of many other FWM-type processes occurring in the nonlinear regime in which a linear stability analysis does not hold. The growth of frequency components in the central region is also related to such FWM processes.

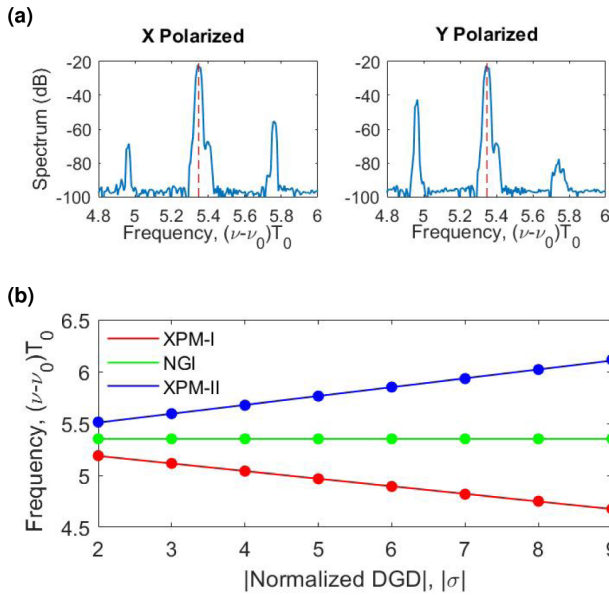


**Fig. 2.** (a) Zoomed view of the first-order sidebands in Fig. 1 generated along the  $x$  and  $y$  axes. (b) Frequencies of the triplet located near  $\Omega/2\pi = 5.4$  in Fig. 1 are plotted as a function of the DGD parameter  $\sigma$ . All other parameters are the same as in Fig. 1. The solid lines show a linear fit to the data. Blue and red curves correspond to the blue and red shifted components of the triplet.

At distances shorter than  $L_{NL}$ , the two XPM sidebands are indeed orthogonally polarized.

As we mentioned earlier, the frequency shift of the XPM-induced triplet depends on the DGD parameter  $\sigma$  and should become larger for its larger values. Numerical simulations, as well as the eigenvalues of the matrix  $M$  in Eq. (22), confirm this expectation. In Fig. 2, we show the three frequencies as a function of  $\sigma$  for the triplet located near  $\Omega/2\pi = 5.4$  in Fig. 1. As one may expect, the frequency the NGI sideband (middle line) is not impacted by the DGD. In contrast, the frequency shift of XPM sidebands increases with  $\sigma$  in a linear fashion. However, the slopes are slightly different in Fig. 2 for the blue and red shifted components. If we represent this shift by  $\delta_{\pm}$  for the two components, we can fit the data with the simple relation  $\delta_{\pm} = S_{\pm}\sigma$ , where  $S_{+} = 0.086$ , and  $S_{-} = -0.073$ . The reason behind the different slopes is related to the presence of  $\sigma$  in the definition of  $A = \sigma\Omega/2$  in Eq. (22). Physically speaking, the dispersion relations are different for the two XPM sidebands because of DGD.

One may ask how the spectra in Figs. 1 and 2 change for negative values of the DGD parameter  $\sigma$ . Our results show that the two XPM-induced sidebands of each triplet flip around the central frequency so as to form a mirror image. In other words, the SOP of the XPM sidebands gets flipped. This is expected on physical grounds because a negative DGD implies that slow and fast axes of the birefringent fiber should be interchanged.

The linear stability analysis produces an exponential growth of all MI sidebands at distances shorter than the nonlinear length  $L_{NL}$ . At distances longer than this length, the growth of these sidebands begins to saturate as the system enters the nonlinear regime. We have used numerical simulations in this regime, and the results are shown in Fig. 3 at distances of

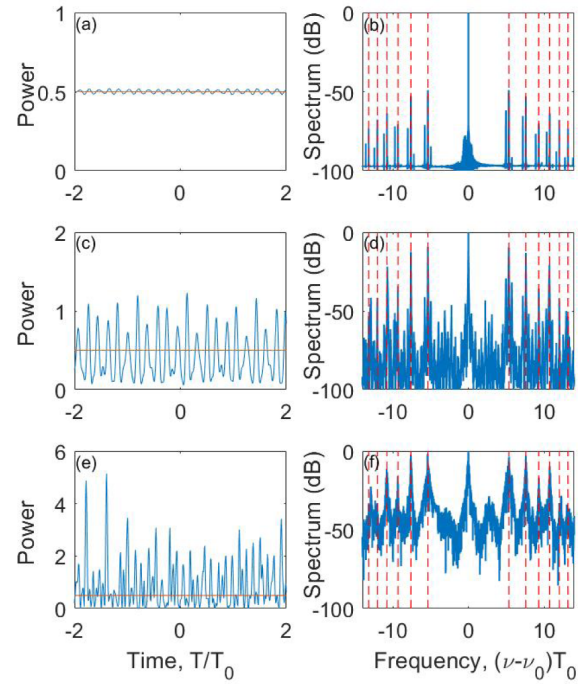


**Fig. 3.** Temporal (left) and spectral (right) patterns of the  $x$ -polarized component of a quasi-CW Gaussian beam at distance of one (top), two (middle), and three (bottom) nonlinear lengths ( $\xi = 1, 2, 3$ ). All other parameters are the same as in Fig. 1. The horizontal lines (left column) indicate input power traces, and vertical dashed red lines (right column) indicate frequencies of the NGI sidebands.

$z/L_{NL} = 1, 2$ , and 3. Only the  $x$ -polarized component is shown because the  $y$ -polarized component behaves in a qualitatively similar manner. In each case, the temporal trace is shown on the left and the corresponding spectrum on the right. At a distance of  $z/L_{NL} = 1$ , the system is in the linear regime, and the MI leads to weak temporal modulation of the CW beam because of the onset of multiple MI sidebands seen on the right side. At a distance  $z/L_{NL} = 2$  (middle row in Fig. 3), the system has entered the nonlinear regime. The spectrum shows that many other sidebands have formed through other FWM-type processes, not accounted for by the linear stability analysis. In the time domain, the amplitude of modulations has become so large that the CW beam has been converted into an irregular pulse train. At a distance  $z/L_{NL} = 3$  (bottom row in Fig. 3), the pulse train becomes almost chaotic because of much larger amplitudes and bandwidths of all MI sidebands located at widely different frequencies. The sideband triplets are no longer discernible and appear to merge to form much wider sidebands.

We have also studied the evolution of a pulsed Gaussian beam inside a GRIN fiber. We keep all parameters the same as in Fig. 3 and solve Eqs. (14) and (15) numerically with the input  $U_j(0, \tau) = 0.5 \text{sech}(\tau T_0/T_p)$  for  $j = x, y$ . The results are shown in Fig. 4 at a distance of  $z/L_{NL} = 5$  using  $T_p = 1$  ps. Top and bottom rows show the temporal and spectral profiles for the  $x$ - and  $y$ -polarized components of the pulse, respectively. The temporal profiles develop considerable high-frequency oscillations because of the onset of the NGI and XPM sidebands seen in the spectrum on the right side. The shifted nature of

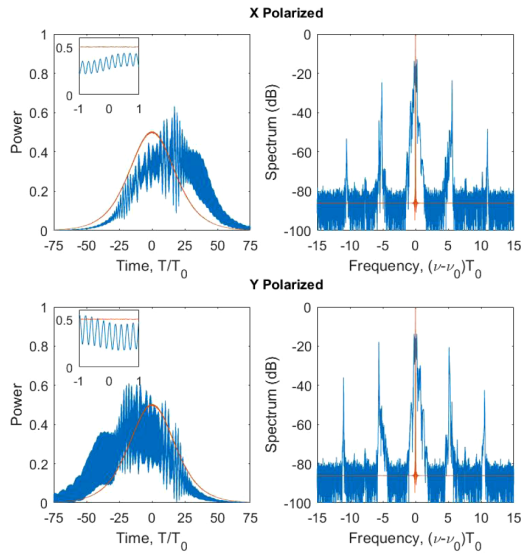


**Fig. 4.** Temporal (left) and spectral (right) profiles of a 1 ps input pulse at a distance of  $z = 5L_{NL}$  for the  $x$ - (top) and  $y$ -polarized (bottom) components of a pulsed Gaussian beam. All other parameters are the same as in Fig. 1. Input profiles (red traces) are shown for comparison.

these profiles indicates that the two polarization components propagate with different group velocities, as dictated by the fiber's DGD, which is taken into account by using  $\sigma = 5$ .

The spectral profiles show several interesting features. First, the central peak is broadened considerably compared to the input spectrum because of SPM. Second, only a few sidebands are generated on the opposite sides of this central peak. Third, the locations of these sidebands are close to but do not match precisely with the NGI-sideband frequencies given in Eq. (24). Fourth, a closer inspection of the temporal profiles reveals that the pulse exhibits rapid oscillations at a high frequency corresponding to the sidebands generated at about  $\Omega/(2\pi) = 5$  (as shown in the insets), but its envelope is also slowly modulated at a much smaller frequency that is related to the XPM-induced sidebands discussed earlier in this section.

## 5. VECTOR MI: ANOMALOUS GVD

In this section, we discuss how the MI behavior changes when the Gaussian beam is launched at a wavelength such that it experiences anomalous GVD inside the GRIN fiber. We can still use Eqs. (14) and (15) with the only change  $s = -1$ . The stability matrix in Eq. (22) remains valid after this change. In the scalar case, the NGI sideband frequencies are predicted by Eq. (24). Using  $s = -1$  in this equation, these frequencies are given by

$$\Omega_p = \pm \sqrt{2(c_0 P_j - \pi q p)}, \quad (j = x, y), \quad p = 0, -1, -2, \dots \quad (25)$$

Note that  $p$  can take only a negative value to ensure that  $\Omega_p$  is a real quantity. As  $q$  is a large number in practice,  $\Omega_p$  is relatively large for all  $p < 0$  compared to the  $p = 0$  sidebands. If we use  $P_j = 1/2$  for a Gaussian beam polarized at  $45^\circ$  from the slow axis, then  $p = 0$  sidebands occur at frequencies given by  $\Omega_p = \pm \sqrt{c_0}$ . This pair does not require a nonlinear grating and

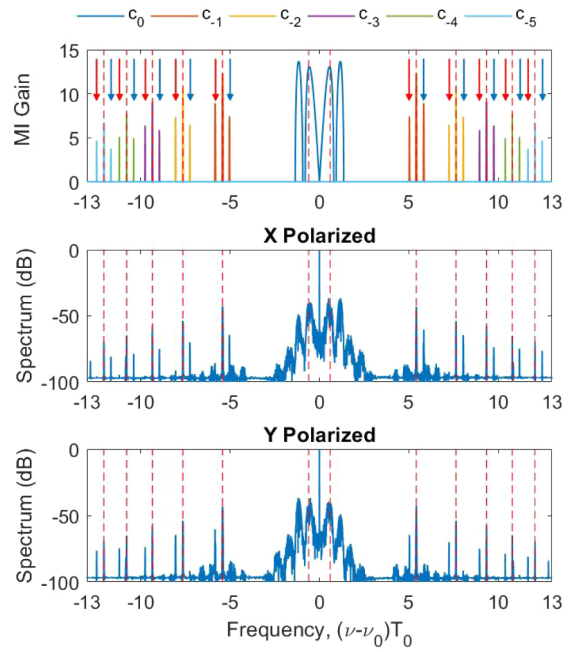


**Fig. 5.** MI Gain spectrum (top) for a Gaussian beam propagating in the anomalous-GVD region of a birefringent GRIN fiber ( $s = -1$ ). Numerical results are shown below for the  $x$ - (middle) and  $y$ - (bottom) polarized components at a distance of  $z = L_{NL}$ . All other features are identical to those in Fig. 1, where the normal-GVD case is shown.

occurs even in step-index fibers. All other sidebands need this grating and occur only for GRIN fibers. Their frequencies are much larger and are also slightly different from those found in the case of normal GVD because of a sign change of the second term for  $p < 0$ .

To study the impact of a fiber's birefringence, we followed the same procedure used in Fig. 1. The results are shown in Fig. 5 after a quasi-CW Gaussian beam has propagated a distance of one nonlinear length ( $\xi = 1$ ). The sideband frequencies shown in the top part were obtained using  $p = 0, -1, -2, -3, -4, -5$  in the stability matrix given in Eq. (22). The most dramatic new feature in the anomalous-GVD case is the generation of two pairs of sidebands near the center. Only one pair is predicted by Eq. (25). The second pair has its origin in the fiber's birefringence. All other sidebands split into a triplet, a feature identical to that found in the case of normal GVD. This splitting again depends on the DGD parameter  $\sigma$  and varies with it in a linear fashion as shown in Fig. 3. Temporal evolution in the case of anomalous GVD is also similar to that seen for the normal-GVD case in Fig. 3. The main difference is that temporal modulations become deeper at shorter distances and evolve into a pulse train whose individual pulses behave as solitons that are known to form in the case of anomalous GVD [1].

To show the formation of solitons in the anomalous-GVD region, we show in Fig. 6 the temporal evolution of the  $x$ - and  $y$ -polarized components of a pulsed Gaussian input beam. We keep the values of all parameters the same as in Fig. 5 and solve Eqs. (14) and (15) numerically using  $s = -1$  and the input  $U_j(0, \tau) = 0.5 \operatorname{sech}(\tau T_0/T_p)$  for  $j = x, y$ , with  $T_p = 1$  ps.

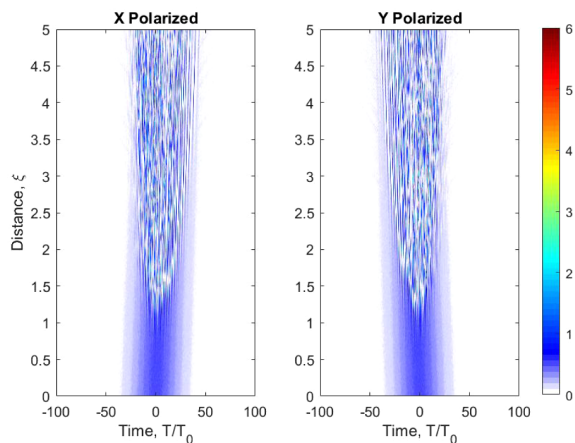


**Fig. 6.** Temporal evolution of 1 ps sech pulse over  $\xi = 5$  in the anomalous-GVD region ( $s = -1$ ). All other parameters are the same as in Fig. 4.

Similar to the normal-GVD case, the two polarization components travel at different speeds because of DGD and change little over a distance of one nonlinear length, except for developing weak oscillations. However, these oscillations become deeper after that distance, and both polarization components evolve into a train of solitons of different widths and peak powers. This behavior also occurs in step-index fibers, but solitons are much narrower in the case of GRIN fibers because of the much larger frequency shifts of the NGI sidebands for them. As the width of these solitons is related to the time scale  $T_0 = 43$  fs for our simulations, higher-order effects such as third-order dispersion and the Raman-induced frequency shift should be included for a more accurate study of such solitons.

## 6. DISCUSSION AND CONCLUSION

We have theoretically investigated MI occurring inside a birefringent GRIN fiber when the two polarization components of the incident optical field are coupled nonlinearly through the nonlinear phenomenon of XPM. When the input beam is launched along the slow or fast axis of this fiber, only modes of one polarization are excited. The scalar theory developed earlier can be applied in this case, and the geometric parametric instability produces an infinite number of sidebands around the wavelength of the input optical beam (called NGI sidebands in this paper). We have found that each of these sidebands splits into a triplet because of XPM-induced coupling between the two polarization components (called XPM sidebands in this paper). We used a linear stability analysis to develop a  $4 \times 4$  stability matrix whose eigenvalues predict the frequencies of both the NGI and XPM sidebands and also provide the gain experienced by these sidebands. In addition, eigenvectors of this matrix were used to find the SOP of each sideband. Our results show that the frequency spacing of each triplet depends on the DGD parameter linearly. We also found that the red and blue shifted components of the triplet are polarized orthogonally, whereas the central component has the same SOP as the input beam.

We verified the predictions of the linear stability analysis numerically by solving two coupled NLS equations that include

spatial self-imaging effects through an effective nonlinear parameter. We present results for both continuous and pulsed optical beams experiencing normal or anomalous GVD inside a GRIN fiber. We have also studied the evolution of MI in the nonlinear regime beyond the linear stability analysis by increasing the propagation distance up to three nonlinear lengths. As expected, temporal modulations become deeper and irregular with increasing distance. In the case of anomalous GVD, these modulations turn into a train of short solitons. We have studied this behavior by considering a pulsed Gaussian beam containing 1 ps wide pulses. Our study adds to the growing literature on the nonlinear effects occurring inside GRIN fibers, and our results should prove useful for applications where birefringent GRIN fibers are needed.

**Funding.** National Science Foundation (ECCS-1933328).

**Disclosures.** The authors declare no conflicts of interest.

## REFERENCES

- G. P. Agrawal, *Nonlinear Fiber Optics*, 6th ed. (Academic, 2019).
- G. P. Agrawal, "Self-imaging in multimode graded-index fibers and its impact on the nonlinear phenomena," *Opt. Fiber Technol.* **50**, 309–316 (2019).
- S. Longhi, "Modulational instability and space time dynamics in nonlinear parabolic-index optical fibers," *Opt. Lett.* **28**, 2363–2365 (2003).
- L. G. Wright, D. N. Christodoulides, and F. W. Wise, "Controllable spatiotemporal nonlinear effects in multimode fibre," *Nat. Photonics* **9**, 306–310 (2015).
- K. Krupa, A. Tonello, A. Barthélémy, V. Couderc, B. M. Shalaby, A. Bendahmane, G. Millot, and S. Wabnitz, "Observation of geometric parametric instability induced by the periodic spatial self-imaging of multimode waves," *Phys. Rev. Lett.* **116**, 183901 (2016).
- K. Krupa, V. Couderc, A. Tonello, A. Picozzi, A. Barthélémy, G. Millot, and S. Wabnitz, "Spatiotemporal nonlinear dynamics in multimode fibers," in *Nonlinear Guided Wave Optics*, S. Wabnitz, ed. (IOP Science, 2017), Chap. 14.
- H. E. Lopez-Aviles, F. O. Wu, Z. S. Eznavneh, M. A. Eftekhari, F. Wise, R. A. Correa, and D. N. Christodoulides, "A systematic analysis of parametric instabilities in nonlinear parabolic multimode fibers," *APL Photon.* **4**, 022803 (2019).
- M. Guasoni, "Generalized modulational instability in multimode fibers: wideband multimode parametric amplification," *Phys. Rev. A* **92**, 033849 (2015).
- L. Li, J. Leng, P. Zhou, and J. Chen, "Modulation instability induced by intermodal cross-phase modulation in step-index multimode fiber," *Appl. Opt.* **58**, 4283–4287 (2019).
- R. Dupiol, A. Bendahmane, K. Krupa, J. Fatome, A. Tonello, M. Fabert, V. Couderc, S. Wabnitz, and G. Millot, "Intermodal modulational instability in graded-index multimode optical fibers," *Opt. Lett.* **42**, 3419–3422 (2017).
- C. M. Arabi, A. Kudlinski, A. Mussot, and M. Conforti, "Geometric parametric instability in periodically modulated graded-index multimode fibers," *Phys. Rev. A* **97**, 023803 (2018).
- J. Rothenberg, "Modulational instability for normal dispersion," *Phys. Rev. A* **42**, 682–685 (1990).
- P. D. Drummond, T. A. B. Kennedy, J. M. Dudley, R. Leonhardt, and J. D. Harvey, "Cross-phase modulational instability in high-birefringence fibers," *Opt. Commun.* **78**, 137–142 (1990).
- F. Biancalana and D. V. Skryabin, "Vector modulational instabilities in ultra-small core optical fibres," *J. Opt.* **A 6**, 301–306 (2004).
- D. Amans, E. Brainis, M. Haelterman, P. Emplit, and S. Massar, "Vector modulation instability induced by vacuum fluctuations in highly birefringent fibers in the anomalous-dispersion regime," *Opt. Lett.* **30**, 1051–1053 (2005).

16. A. Tonello, S. Pitois, S. Wabnitz, G. Millot, T. Martynkien, W. Urbanczyk, J. Wojcik, A. Locatelli, M. Conforti, and C. De Angelis, "Frequency tunable polarization and intermodal modulation instability in high birefringence holey fiber," *Opt. Express* **14**, 397–404 (2006).
17. J. S. Y. Chen, G. K. L. Wong, S. G. Murdoch, R. J. Kruhlak, R. Leonhardt, J. D. Harvey, N. Y. Joly, and J. C. Knight, "Cross-phase modulation instability in photonic crystal fibers," *Opt. Lett.* **31**, 873–875 (2006).
18. M. B. Shemirani, W. Mao, R. A. Panicker, and J. M. Kahn, "Principal modes in graded-index multimode fiber in presence of spatial- and polarization-mode coupling," *J. Lightwave Technol.* **27**, 1248–1261 (2009).
19. M. Conforti, C. M. Arabi, A. Mussot, and A. Kudlinski, "Fast and accurate modeling of nonlinear pulse propagation in graded-index multimode fibers," *Opt. Lett.* **42**, 4004–4007 (2017).
20. M. Karlsson, D. Anderson, and M. Desaix, "Dynamics of self-focusing and self-phase modulation in a parabolic index optical fiber," *Opt. Lett.* **17**, 22–24 (1992).
21. F. Matera, A. Mecozzi, M. Romagnoli, and M. Settembre, "Sideband instability induced by periodic power variation in long-distance fiber links," *Opt. Lett.* **18**, 1499–1501 (1993).
22. J. Hult, "A fourth-order Runge–Kutta in the interaction picture method for simulating supercontinuum generation in optical fibers," *J. Lightwave Technol.* **25**, 3770–3775 (2007).